Available online at www.sciencedirect.com
ScienceDirect
Journal of Computational Physics 224 (2007) 1223–1242
JOURNAL OF COMPUTATIONAL PHYSICS
www.elsevier.com/locate/jcp

A Runge–Kutta discontinuous Galerkin method for viscous flow equations

Hongwei Liu, Kun Xu *

Mathematics Department, Hong Kong University of Science and Technology, Clear Water Bay, Kowloon, Hong Kong 10000, China

Received 14 October 2005; received in revised form 18 October 2006; accepted 13 November 2006
Available online 12 January 2007

Abstract

This paper presents a Runge–Kutta discontinuous Galerkin (RKDG) method for viscous flow computation. The construction of the RKDG method is based on a gas-kinetic formulation, which not only couples the convective and dissipative terms together, but also includes both discontinuous and continuous representation in the flux evaluation at a cell interface through a simple hybrid gas distribution function. Due to the intrinsic connection between the gas-kinetic BGK model and the Navier–Stokes equations, the Navier–Stokes flux is automatically obtained by the present method. Numerical examples for both one dimensional (1D) and two dimensional (2D) compressible viscous flows are presented to demonstrate the accuracy and shock capturing capability of the current RKDG method.

Keywords: Discontinuous Galerkin method; Gas-kinetic scheme; Viscous flow simulations

1. Introduction

In the past decades, both the finite volume (FV) and the discontinuous Galerkin (DG) finite element methods have been successfully developed for the compressible flow simulations. Most FV schemes use piecewise constant representation for the flow variables and employ the reconstruction techniques to obtain high accuracy. A higher-order scheme usually has a larger stencil than a lower-order scheme, which makes it difficult to be applied on unstructured mesh or complicated geometry. For the DG method high-order accuracy is obtained by means of high-order approximation within each element, where more information is stored for each element during the computation. The compactness of the DG method allows it to deal with unstructured mesh or complicated geometry easily. Now the DG method has served as a high-order method for a broad class of engineering problems [6].

For viscous flow problems, many successful DG methods have been proposed in the literature, such as those by Bassi and Rebay [1], Cockburn and Shu [11], Baumann and Oden [14], and many others. In [5], a

* Corresponding author. Tel.: +852 2358 7433; fax: +852 2358 1643.
E-mail addresses: hwliu@ust.hk (H. Liu), makxu@ust.hk (K. Xu).

0021-9991/$ - see front matter © 2006 Elsevier Inc. All rights reserved.
doi:10.1016/j.jcp.2006.11.014

large class of discontinuous Galerkin methods for second-order elliptic problems have been analyzed in a unified framework. More recently, van Leer and Nomura [22] proposed a recovery-based DG method for diffusion equation using the recovery principle. This method has deep physical insight in the construction of a DG method for convection–diffusion problem.

The RKDG method for non-linear convection-dominated problems was first proposed and studied by Cockburn, Shu and their collaborators in a series of papers [7–11], see [12] for a review of the method. The excellent results obtained by the high-order accurate RKDG method demonstrated itself as a powerful tool in the computational fluid dynamics. Recently, the gas-kinetic RKDG method proposed by Tang and Warnecke [15] has been shown to be very accurate and efficient for inviscid flow simulations.

In this paper, a RKDG method for the viscous flow problems based on a gas-kinetic formulation will be presented. Instead of treating the convection and dissipation effects separately, we use the gas-kinetic distribution function with both inviscid and viscous terms in the construction of the numerical flux at the cell interface. Due to the intrinsic connection between the gas-kinetic BGK model and the Navier–Stokes equations, the Navier–Stokes flux is automatically obtained by the RKDG method. The numerical dissipation introduced from the discontinuity at the cell interface is favored by the inviscid flow calculation, especially for the capturing of numerical shock fronts. For viscous flow problems, it should be avoided because the artificial viscosity from the discontinuity deteriorates the physical one [24]. A simplified gas-kinetic relaxation model, which plays the role of recovering the continuity of the flow variables from the initial discontinuous representation, will be used in the present method. In [28], the DG-BGK method has been developed which gives accurate solutions in both high and low Reynolds number flow simulations. The spirit of the present RKDG method in the construction of the viscous numerical flux is similar to that of the DG-BGK method but with some significant modification and simplification. The RKDG method uses Runge–Kutta or TVD-RK [19] method for the temporal discretization and the DG-BGK method integrates the viscous flow equations in time directly. In the DG-BGK method, only one-dimensional scheme was presented. However, in this paper the multidimensional RKDG method will be constructed as well. More importantly, the RKDG method for the viscous flows is more accurate than the DG-BGK method, which is demonstrated by the numerical tests.

The outline of this paper is as follows. In Section 2 we describe the RKDG method for the viscous flow equations. The one-dimensional formulation is given in detail in the first two subsections, then the extension to multidimensional cases is described. The limiting procedure and boundary conditions are also presented in Section 2. The performance of the method is illustrated in Section 3 by six numerical examples including both 1D and 2D problems. Section 4 is the conclusion.

2. Runge–Kutta discontinuous Galerkin method

For the compressible flow simulations, a finite volume gas-kinetic BGK scheme has been developed and applied to many physical and engineering problems [24]. Similar to many other finite volume methods, the gas-kinetic scheme is mainly about the flux evaluation at the cell interface. The distinguishable feature of the gas-kinetic BGK scheme is that a Navier–Stokes flux is given directly from the MUSCL-type reconstructed initial data [21], where both slopes at each cell interface participate the gas evaluation. In the RKDG method [12], a high-order approximate solution inside a cell is updated automatically and limited carefully to enforce the stability and to suppress the numerical oscillations. In this section, we will present the RKDG method for the Navier–Stokes equations by incorporating the gas-kinetic formulation.

2.1. DG spatial discretization in 1D case

For a 1D flow, the BGK model in the x-direction is [3]

$$f_t + uf_x = \frac{g - f}{\tau}, \tag{2.1}$$

where u is the particle velocity, f is the gas distribution function and g is the equilibrium state approached by f. The particle collision time τ is related to the viscosity and heat conduction coefficients. The equilibrium state is a Maxwellian distribution,

$$g = \rho\left(\frac{\lambda}{\pi}\right)^{\frac{K+1}{2}} \mathrm{e}^{-\lambda[(u-U)^2+\xi^2]}, \tag{2.2}$$

where ρ is the density, U is the macroscopic velocity and λ is related to the gas temperature T by $\lambda = m/2kT$, where m is the molecular mass, and k is the Boltzmann constant. The total number of degree of freedom K in ξ is equal to $(5-3\gamma)/(\gamma-1)+2$. In the above equilibrium state g, ξ^2 is equal to $\xi^2 = \xi_1^2 + \xi_2^2 + \cdots + \xi_K^2$. The relation between the macroscopic variables and the microscopic distribution functions is

$$\mathbf{W} = (\rho, \rho U, \rho E)^{\mathrm{T}} = \int \psi f \,\mathrm{d}\Xi = \int \psi g \,\mathrm{d}\Xi, \tag{2.3}$$

where ψ is the vector of moments

$$\psi = \left(1, u, \frac{1}{2}(u^2+\xi^2)\right)^{\mathrm{T}}, \tag{2.4}$$

and $\mathrm{d}\Xi = \mathrm{d}u\mathrm{d}\xi$ is the volume element in the phase space with $\mathrm{d}\xi = \mathrm{d}\xi_1\mathrm{d}\xi_2\cdots\mathrm{d}\xi_K$. The compatibility condition can be obtained from Eq. (2.3), i.e.,

$$\int \psi \frac{g-f}{\tau}\,\mathrm{d}\Xi = 0, \tag{2.5}$$

where τ is assumed to be independent of individual particle velocity. Based on the above BGK model, the corresponding Navier–Stokes equations can be derived. The advantage of using the BGK equation instead of the Navier–Stokes equations is that it is a first-order differential equation with a relaxation term.

By taking the moments of ψ to Eq. (2.1), due to the compatibility condition (2.5), we have

$$\frac{\partial}{\partial t}\int \psi f \,\mathrm{d}\Xi + \frac{\partial}{\partial x}\int u\psi f \,\mathrm{d}\Xi = 0 \tag{2.6}$$

or

$$\mathbf{W}_t + \mathbf{G}_x = 0, \tag{2.7}$$

where $\mathbf{G} = \int u\psi f \,\mathrm{d}\Xi$ is the flux for the corresponding conservative variables $\mathbf{W} = \int \psi f \,\mathrm{d}\Xi$. To the first order of τ, the Chapman–Enskog expansion shows that Eq. (2.7) corresponds to the one-dimensional Navier–Stokes equations. Note that f in Eq. (2.6) will include both equilibrium and non-equilibrium parts in a Chapman–Enskog expansion. Therefore, the flux $\mathbf{G}$ will contain both inviscid and viscous terms accordingly.

For a given partition in 1D space, we denote the cells by $I_i = \left[x_{i-\frac{1}{2}}, x_{i+\frac{1}{2}}\right]$ and choose the local Legendre polynomials $\phi_i^l(x)$ as the basis functions, then the approximate solution $\mathbf{W}^h$ can be expressed as

$$\mathbf{W}^h(x,t) = \sum_{l=0}^{k} \mathbf{W}_i^l(t)\phi_i^l(x) \quad \text{for } x \in I_i. \tag{2.8}$$

The initial value of $\mathbf{W}_i^l(0)$ can be obtained by

$$\mathbf{W}_i^l(0) = \frac{2l+1}{\Delta x_i}\int_{I_i} \mathbf{W}_0(x)\phi_i^l(x)\,\mathrm{d}x \tag{2.9}$$

for $l = 0,\ldots,k$, where $\Delta x_i = x_{i+1/2} - x_{i-1/2}$ and $\mathbf{W}_0(x)$ is the initial condition. In order to determine the time-dependent approximate solution, as given in [8], we can enforce Eq. (2.7) cell by cell by means of a Galerkin method. More specifically, for each cell I_i, we get

$$\frac{\mathrm{d}}{\mathrm{d}t}\mathbf{W}_i^l(t) + \frac{2l+1}{\Delta x_i}\left(\widehat{\mathbf{G}}_{i+\frac{1}{2}} - (-1)^l\widehat{\mathbf{G}}_{i-\frac{1}{2}}\right) = \frac{2l+1}{\Delta x_i}\int_{I_i}\mathbf{G}(x,t)\frac{\mathrm{d}}{\mathrm{d}x}(\phi_i^l(x))\,\mathrm{d}x \tag{2.10}$$

for $l = 0,\ldots,k$, where $\widehat{\mathbf{G}}_{i+\frac{1}{2}}$ is the flux at $x_{i+\frac{1}{2}}$, i.e., $\widehat{\mathbf{G}}_{i+\frac{1}{2}} = \int u\psi f(x_{i+\frac{1}{2}},t,u,\xi)\,\mathrm{d}\Xi$, and $\mathbf{G}(x,t)$ is the flux inside each cell. Eq. (2.10) is the system of ODEs for the degrees of freedom $\mathbf{W}_i^l(t)$ which can be solved by the Runge–Kutta (RK) or the TVD-RK time stepping methods [19]. Given the continuous flow states inside the cells, we could use $\mathbf{G} = \int u\psi f \,\mathrm{d}\Xi$ to calculate the integral on the right hand side of Eq. (2.10) by the Gaussian rule

consistent with the accuracy requirement for Navier–Stokes solutions. In order to save the computational cost, we have also used the flux of the macroscopic Navier–Stokes equations corresponding to Eq. (2.7) directly. Both of them work equally well in our numerical tests. In the following, we are going to present the flux evaluation at the cell interface $x_{i+\frac{1}{2}}$ based on the gas-kinetic formulation for the viscous flow equations.

2.2. Gas-kinetic flux evaluation at a cell interface

In the finite volume BGK scheme [24], the flux at the cell interface is evaluated based on the integral solution f of the BGK model (2.1),

$$f(x_{i+1/2},t,u,\xi)=\frac{1}{\tau}\int_0^t g(x',t',u,\xi)\mathrm{e}^{-(t-t')/\tau}\,\mathrm{d}t'+\mathrm{e}^{-t/\tau}f_0(x_{i+1/2}-ut), \tag{2.11}$$

where $x'=x_{i+1/2}-u(t-t')$ is the trajectory of a particle motion and f_0 is the initial gas distribution function at the beginning of each time step ($t=0$). The integration part on the right hand side of Eq. (2.11) is the gain term due to the particle collision. In order to figure out the gas distribution function at the cell interface $x_{i+1/2}$, two unknowns g and f_0 in the above equation must be specified, see [24] for some details.

The time-dependent viscous flux given by the BGK scheme is accurate up to the order of $O(\tau\Delta t^2)$ in smooth regions [16]. In order to construct a simple formula of the numerical flux for the RKDG method, we consider the hybridization of the loss and gain terms in the gas distribution function in the present work. Similar to other hybrid schemes, the BGK scheme presented in Eq. (2.11) can be further simplified. As shown in [23], for the Navier–Stokes solutions the distribution function at the cell interface can be constructed as

$$f=[1-\mathscr{L}(\cdot)]f_0+\mathscr{L}(\cdot)f_c, \tag{2.12}$$

where f_0 is the initial distribution function in Eq. (2.11). This is also the so-called kinetic flux-vector splitting Navier–Stokes (KFVS-NS) distribution function proposed by Chou and Baganoff [4]. In Eq. (2.12) f_c is the distribution function due to the collision effect, and $\mathscr{L}(\cdot)$ is the relaxation parameter to determine the speed that a system evolves into an equilibrium state and should be a function of local flow variables, such as the flow jump around the cell interface. Inherently, the free transport mechanism in f_0 uses the time step Δt as the particle collision time, the resulting numerical viscosity coefficient is $\mu_{f_0}\simeq p\Delta t$ [26], where p is the pressure. The collision term f_c has the effect of recovering the continuous flow distribution from a discontinuous initial approximate solution, hence it will be helpful to reduce the numerical dissipation introduced in a discontinuity. The principle of the hybridization is as follows. The relaxation parameter $\mathscr{L}(\cdot)$ should be determined in such a way that the contribution of f_0 becomes dominant in the non-equilibrium flow regions to provide enough numerical dissipation while the physical scale cannot be resolved by the cell size. The term f_c contributes more in smooth regions to recover the physical dissipative effect.

There are many ways to construct the relaxation parameter $\mathscr{L}(\cdot)$, see examples in [23,25]. In this paper, one choice of $\mathscr{L}(\cdot)$ is given. As we know, for shock wave, the distribution function will stay in a non-equilibrium state along with the pressure jumps across the shock, hence the parameter $\mathscr{L}(\cdot)$ can be designed as a function of the local pressure jumps around the cell interface, which is

$$\mathscr{L}(\cdot)=\exp\left[-C\frac{\left|p^{\mathrm{l}}_{i+1/2}-p^{\mathrm{r}}_{i+1/2}\right|}{p^{\mathrm{l}}_{i+1/2}+p^{\mathrm{r}}_{i+1/2}}\right], \tag{2.13}$$

where $p^{\mathrm{l,r}}_{i+1/2}$ are the left and right values of pressure p at the cell interface $x_{i+1/2}$. Theoretically, C should depend on the physical solution, the numerical jumps at the cell interface, and the cell size. Currently, it is still hard to give a general formulation for it. Therefore, in this paper C is a problem-dependent positive constant which ranges from 10^3 to 10^5 in our computation. In the regions with large pressure gradients, for example in the numerical shock layer, when the shock is under-resolved, a small value of $\mathscr{L}(\cdot)$ should be used to add more numerical dissipation through the amplification of f_0. In this case, the numerical shock layer constructed will be much wider than the physical one. On the other hand, if the shock structure is well-resolved, the distribution function f_c should be the dominant part. A similar switch function is also employed in the high-resolution gas-kinetic schemes by Ohwada and Fukata [17].

In the FV BGK method [24], the initial macroscopic flow variables around a cell interface are reconstructed by the MUSCL-type interpolation. But, for the RKDG method, they are updated inside each cell. In the following, the location of the cell interface $x_{i+1/2} = 0$ will be used for simplicity. With the initial macroscopic flow states on both sides of a cell interface, to the Navier–Stokes order the initial gas distribution function f_0 is constructed as

$$f_0 = \begin{cases} g^{\mathrm{l}}[1 + a^{\mathrm{l}}x - \tau(a^{\mathrm{l}}u + A^{\mathrm{l}})], & x \leqslant 0, \\ g^{\mathrm{r}}[1 + a^{\mathrm{r}}x - \tau(a^{\mathrm{r}}u + A^{\mathrm{r}})], & x \geqslant 0, \end{cases} \tag{2.14}$$

where g^{l} and g^{r} are the equilibrium states at the left and right hand sides of the cell interface. The Maxwellian distribution functions g^{l} and g^{r} have unique correspondence with the macroscopic variables there, i.e.,

$$g^{\mathrm{l}} = g^{\mathrm{l}}\left(\mathbf{W}^{\mathrm{l}}_{i+1/2}\right) \quad \text{and} \quad g^{\mathrm{r}} = g^{\mathrm{r}}\left(\mathbf{W}^{\mathrm{r}}_{i+1/2}\right). \tag{2.15}$$

The additional terms $-\tau g^{\mathrm{l}}(a^{\mathrm{l}}u + A^{\mathrm{l}})$ and $-\tau g^{\mathrm{r}}(a^{\mathrm{r}}u + A^{\mathrm{r}})$ are the non-equilibrium parts obtained from the Chapman–Enskog expansion of the BGK model, which account for the dissipative effects. Here a^{l} and a^{r} in Eq. (2.14) are coming from the spatial derivatives of the Maxwellian distribution functions, i.e.,

$$a^{\mathrm{l}} = a^{\mathrm{l}}_1 + a^{\mathrm{l}}_2 u + \frac{1}{2}a^{\mathrm{l}}_3(u^2 + \xi^2) \quad \text{and} \quad a^{\mathrm{r}} = a^{\mathrm{r}}_1 + a^{\mathrm{r}}_2 u + \frac{1}{2}a^{\mathrm{r}}_3(u^2 + \xi^2), \tag{2.16}$$

which can be uniquely evaluated from the spatial derivatives of the conservative variables at the left and right hand sides of the cell interface. Since there is no contribution in the mass, momentum and energy from the non-equilibrium parts, the parameters in $A^{\mathrm{l}} = A^{\mathrm{l}}_1 + A^{\mathrm{l}}_2 u + \frac{1}{2}A^{\mathrm{l}}_3(u^2 + \xi^2)$ and $A^{\mathrm{r}} = A^{\mathrm{r}}_1 + A^{\mathrm{r}}_2 u + \frac{1}{2}A^{\mathrm{r}}_3(u^2 + \xi^2)$ are uniquely determined by the compatibility condition

$$\int \psi g^{\mathrm{l}}(a^{\mathrm{l}}u + A^{\mathrm{l}})\,\mathrm{d}\Xi = 0 \quad \text{and} \quad \int \psi g^{\mathrm{r}}(a^{\mathrm{r}}u + A^{\mathrm{r}})\,\mathrm{d}\Xi = 0. \tag{2.17}$$

Even though the non-equilibrium parts have no contribution to the conservative flow variables (moments of ψ), they do have contribution to the flux (moments of $u\psi$). Note that for the initial distribution function f_0, both the state and the derivative have discontinuities at the cell interface.

The distribution function f_{c} due to the collision effect can be constructed as

$$f_{\mathrm{c}} = g_0[1 - \tau(u\bar{a}^{\mathrm{l}}H[u] + u\bar{a}^{\mathrm{r}}(1 - H[u]) + \bar{A})], \tag{2.18}$$

where $H[u]$ is the Heaviside function, and g_0 is a local Maxwellian distribution function located at $x = 0$. The dependence of $\bar{a}^{\mathrm{l}}$, $\bar{a}^{\mathrm{r}}$ and $\overline{A}$ on the particle velocities are also coming from a Taylor expansion of a Maxwellian distribution, which have the forms $\bar{a}^{\mathrm{l}} = \bar{a}^{\mathrm{l}}_1 + \bar{a}^{\mathrm{l}}_2 u + \frac{1}{2}\bar{a}^{\mathrm{l}}_3(u^2 + \xi^2)$, $\bar{a}^{\mathrm{r}} = \bar{a}^{\mathrm{r}}_1 + \bar{a}^{\mathrm{r}}_2 u + \frac{1}{2}\bar{a}^{\mathrm{r}}_3(u^2 + \xi^2)$ and $\bar{A} = \overline{A}_1 + \overline{A}_2 u + \frac{1}{2}\overline{A}_3(u^2 + \xi^2)$. The determination of the parameters in Eq. (2.18) is as follows. The equilibrium state g_0 at the cell interface is constructed from the conservation constraint,

$$\mathbf{W}_0 = \int \psi g_0\,\mathrm{d}\Xi = \int_{u>0} \psi g^{\mathrm{l}}\,\mathrm{d}\Xi + \int_{u<0} \psi g^{\mathrm{r}}\,\mathrm{d}\Xi. \tag{2.19}$$

For the distribution function f_{c}, the terms related to the spatial and temporal gradients have to be constructed as well. In the smooth flow cases, we can use the following relation to calculate a continuous derivative $\bar{a} = \bar{a}^{\mathrm{l}} = \bar{a}^{\mathrm{r}}$ of g_0:

$$\int \psi g_0 \bar{a}\,\mathrm{d}\Xi = \int_{u>0} \psi g^{\mathrm{l}} a^{\mathrm{l}}\,\mathrm{d}\Xi + \int_{u<0} \psi g^{\mathrm{r}} a^{\mathrm{r}}\,\mathrm{d}\Xi. \tag{2.20}$$

This relation has been tested in the first two numerical examples. Without using limiter, the high-order accuracy of Eq. (2.20) has been clearly demonstrated. However, for the cases where the limiting procedure is necessary for eliminating the numerical oscillations the following approximation is used:

$$2(\mathbf{W}_0 - \overline{\mathbf{W}}_i)/\Delta x_i = \int \psi g_0 \bar{a}^{\mathrm{l}}\,\mathrm{d}\Xi \quad \text{and} \quad 2\left(\overline{\mathbf{W}}_{i+1} - \mathbf{W}_0\right)/\Delta x_{i+1} = \int \psi g_0 \bar{a}^{\mathrm{r}}\,\mathrm{d}\Xi, \tag{2.21}$$

where two derivatives $\bar{a}^{\mathrm{l}}$ and $\bar{a}^{\mathrm{r}}$ of g_0 are evaluated, and $\overline{\mathbf{W}}_i$ and $\overline{\mathbf{W}}_{i+1}$ are cell average values. Numerically, for the solution with discontinuities, Eq. (2.21) performs better than Eq. (2.20). Although Eq. (2.21) seems to be a second-order spacial approximation, it still works well in the third-order P^2 scheme in our computation for the strongly discontinuous tests. One of the reason for this is that $\mathbf{W}_0$ is constructed through the higher-order approximation of g^{l} and g^{r}. The term $\overline{A}$ in Eq. (2.18) can be uniquely determined from the compatibility condition at the cell interface, i.e.,

$$\int \psi g_0(u\bar{a} + \overline{A})\,\mathrm{d}\Xi = 0 \tag{2.22}$$

for Eq. (2.20), and

$$\int \psi g_0(u\bar{a}^{\mathrm{l}}H[u] + u\bar{a}^{\mathrm{r}}(1 - H[u]) + \overline{A})\,\mathrm{d}\Xi = 0 \tag{2.23}$$

for Eq. (2.21). Note that the distribution function f_{c} plays the role of recovering the continuity from the initial discontinuous representation. This procedure is critically important to capture the viscous solution.

For the Navier–Stokes solutions, the viscosity and heat conduction coefficients are related to the particle collision time τ. With the given dynamical viscosity coefficient μ, the collision time can be calculated by $\tau = \mu/p$, where p is the pressure. Up to this point, we have determined all parameters in the distribution functions f_0 and f_{c}. After substituting Eqs. (2.13), (2.14) and (2.18) into Eq. (2.12), we can get the gas distribution function f at the cell interface, then the numerical flux can be obtained by taking the moments $u\psi$ to it. In order to get the heat conduction correct, the energy flux in Eq. (2.12) can be modified according to the realistic Prandtl number [24].

2.3. Extension to multidimensional cases

The present RKDG method can be easily extended to multidimensional cases. Here we describe the construction of the P^2 scheme for two-dimensional case with rectangular elements. The 2D BGK model can be written as

$$f_t + uf_x + vf_y = \frac{g - f}{\tau}, \tag{2.24}$$

where the equilibrium distribution g is

$$g = \rho\left(\frac{\lambda}{\pi}\right)^{\frac{K+2}{2}} \mathrm{e}^{-\lambda[(u-U)^2+(v-V)^2+\xi^2]}. \tag{2.25}$$

By taking the moments of $\psi = \left(1, u, v, \frac{1}{2}(u^2 + v^2 + \xi^2)\right)^{\mathrm{T}}$ to Eq. (2.24), we can get the governing equation

$$\frac{\partial}{\partial t}\int \psi f\,\mathrm{d}\Xi + \frac{\partial}{\partial x}\int u\psi f\,\mathrm{d}\Xi + \frac{\partial}{\partial y}\int v\psi f\,\mathrm{d}\Xi = 0 \tag{2.26}$$

or

$$\mathbf{W}_t + \mathbf{G}_x + \mathbf{H}_y = 0, \tag{2.27}$$

which correspond to the 2D Navier–Stokes equations when f is approximated to the first order of τ.

For a rectangular cell $I_{i,j} = [x_{i-1/2}, x_{i+1/2}] \times [y_{j-1/2}, y_{j+1/2}]$ in the computational domain, we take the same local basis functions $\phi^{\mathrm{l}}_{i,j}$ as in [10],

$$\begin{aligned} &\phi^0_{i,j}(\mathbf{x}) = 1, \quad \phi^1_{i,j}(\mathbf{x}) = \frac{2(x - x_i)}{\Delta x_i}, \quad \phi^2_{i,j}(\mathbf{x}) = \frac{2(y - y_j)}{\Delta y_j}, \\ &\phi^3_{i,j}(\mathbf{x}) = \phi^1_{i,j}(\mathbf{x})\phi^2_{i,j}(\mathbf{x}), \quad \phi^4_{i,j}(\mathbf{x}) = \left(\phi^1_{i,j}(\mathbf{x})\right)^2 - \frac{1}{3}, \quad \phi^5_{i,j}(\mathbf{x}) = \left(\phi^2_{i,j}(\mathbf{x})\right)^2 - \frac{1}{3}, \end{aligned} \tag{2.28}$$

where $\mathbf{x} \equiv (x, y) \in I_{i,j}$, $\Delta x_i = x_{i+1/2} - x_{i-1/2}$ and $\Delta y_j = y_{j+1/2} - y_{j-1/2}$. Then the approximate solution $\mathbf{W}^h$ inside the element $I_{i,j}$ can be expressed as

$$\mathbf{W}^h(\mathbf{x},t)=\sum_{l=0}^{5}\mathbf{W}_{i,j}^l(t)\phi_{i,j}^l(\mathbf{x})\quad\text{for }\mathbf{x}\in I_{i,j}. \tag{2.29}$$

In order to determine the solution, we need to solve the following weak formulation of Eq. (2.27):

$$\begin{aligned}&\frac{\mathrm{d}}{\mathrm{d}t}\mathbf{W}_{i,j}^l(t)+\frac{1}{a_lS}\left(\int_{y_{j-\frac{1}{2}}}^{y_{j+\frac{1}{2}}}\left(\widehat{\mathbf{G}}\left(x_{i+\frac{1}{2}},y,t\right)\phi_{i,j}^l\left(x_{i+\frac{1}{2}},y\right)-\widehat{\mathbf{G}}\left(x_{i-\frac{1}{2}},y,t\right)\phi_{i,j}^l\left(x_{i-\frac{1}{2}},y\right)\right)\mathrm{d}y\right.\\&\left.+\int_{x_{i-\frac{1}{2}}}^{x_{i+\frac{1}{2}}}\left(\widehat{\mathbf{H}}\left(x,y_{j+\frac{1}{2}},t\right)\phi_{i,j}^l(x,y_{j+\frac{1}{2}})-\widehat{\mathbf{H}}\left(x,y_{j-\frac{1}{2}},t\right)\phi_{i,j}^l\left(x,y_{j-\frac{1}{2}}\right)\right)\mathrm{d}x\right)\\&-\frac{1}{a_lS}\int_{I_{i,j}}\left(\mathbf{G}(x,y,t)\frac{\partial}{\partial x}\phi_{i,j}^l(x,y)+\mathbf{H}(x,y,t)\frac{\partial}{\partial y}\phi_{i,j}^l(x,y)\right)\mathrm{d}x\,\mathrm{d}y=0\end{aligned} \tag{2.30}$$

for $l=0,1,\ldots,5$, where a_l are the normalization constants as shown in [10] and $S=\Delta x_i\Delta y_j$. We use the 3-point Gaussian rule for the edge integral and a tensor product of that with nine quadrature points for the interior integral in Eq. (2.30). Again the flux $\mathbf{G}(x,y,t)$ and $\mathbf{H}(x,y,t)$ inside the element will be calculated from the corresponding Navier–Stokes equations for efficiency consideration. The numerical flux $\widehat{\mathbf{G}}\left(x_{i+\frac{1}{2}},y,t\right)$ and $\widehat{\mathbf{H}}\left(x,y_{j+\frac{1}{2}},t\right)$ at the cell interfaces will be calculated from the gas-kinetic formulation which is presented in the following.

There are two approaches that can be used to construct the numerical flux: one is the directional splitting method [24] and the other is the fully multidimensional method [27]. In this paper we employ the less costly splitting method to construct the flux at the cell interfaces for efficiency and simplicity consideration. For the directional splitting method, only the partial derivatives of the conservative variables in the normal direction of the cell interface will be used in the flux evaluation, which is similar to 1D case. As an illustration, we give the detailed formulae for calculating the flux in the x-direction $\widehat{\mathbf{G}}\left(x_{i+\frac{1}{2}},y_*,t\right)$ at a Gaussian quadrature point $\left(x_{i+\frac{1}{2}},y_*\right)$, and the similar calculations can be done in the y-direction. We will still use Eq. (2.1) with the equilibrium state given by Eq. (2.25) and the simple hybrid distribution function given by Eq. (2.12) to construct the flux $\widehat{\mathbf{G}}\left(x_{i+\frac{1}{2}},y_*,t\right)$. The hybrid parameter $\mathscr{L}(\cdot)$ in Eq. (2.12) is determined by Eq. (2.13) again. With the assumption of $x_{i+\frac{1}{2}}=0$, the initial gas distribution function f_0 in Eq. (2.12) is expressed as

$$f_0=\begin{cases}g^{\mathrm{l}}[1+a^{\mathrm{l}}x-\tau(a^{\mathrm{l}}u+A^{\mathrm{l}})], & x\leqslant 0,\ \ y=y_*,\\ g^{\mathrm{r}}[1+a^{\mathrm{r}}x-\tau(a^{\mathrm{r}}u+A^{\mathrm{r}})], & x\geqslant 0,\ \ y=y_*,\end{cases} \tag{2.31}$$

where g^{l} and g^{r} are the equilibrium states at the left and right hand sides of the quadrature point, a^{l} and a^{r} are expressed as

$$a^{\mathrm{l}}=a_1^{\mathrm{l}}+a_2^{\mathrm{l}}u+a_3^{\mathrm{l}}v+\frac{1}{2}a_4^{\mathrm{l}}(u^2+v^2+\xi^2),\quad a^{\mathrm{r}}=a_1^{\mathrm{r}}+a_2^{\mathrm{r}}u+a_3^{\mathrm{r}}v+\frac{1}{2}a_4^{\mathrm{r}}(u^2+v^2+\xi^2), \tag{2.32}$$

which can be uniquely determined from the partial derivatives of the conservative variables with respect to x there. The terms $A^{\mathrm{l}}=A_1^{\mathrm{l}}+A_2^{\mathrm{l}}u+A_3^{\mathrm{l}}v+\frac{1}{2}A_4^{\mathrm{l}}(u^2+v^2+\xi^2)$ and $A^{\mathrm{r}}=A_1^{\mathrm{r}}+A_2^{\mathrm{r}}u+A_3^{\mathrm{r}}v+\frac{1}{2}A_4^{\mathrm{r}}(u^2+v^2+\xi^2)$ can be calculated from the compatibility condition Eq. (2.17). The collisional distribution function f_{c} in Eq. (2.12) is written as Eq. (2.18), where g_0 is constructed by Eq. (2.19). Similar to 1D case, for the flow problems with smooth solutions, we use the relation of Eq. (2.20) to calculate the continuous derivative $\bar{a}=\bar{a}^{\mathrm{l}}=\bar{a}^{\mathrm{r}}$ of g_0. For the viscous flows with strong discontinuities, the limiting procedure becomes necessary, and the following approximation:

$$2(\mathbf{W}_0-\overline{\mathbf{W}}_{i,j})/\Delta x_i=\int\psi g_0\bar{a}^l\,\mathrm{d}\Xi\quad\text{and}\quad 2(\overline{\mathbf{W}}_{i+1,j}-\mathbf{W}_0)/\Delta x_{i+1}=\int\psi g_0\bar{a}^{\mathrm{r}}\,\mathrm{d}\Xi \tag{2.33}$$

are used to obtain $\bar{a}^{\mathrm{l}}$ and $\bar{a}^{\mathrm{r}}$ in Eq. (2.18), where $\overline{\mathbf{W}}_{i,j}$ and $\overline{\mathbf{W}}_{i+1,j}$ are cell average values. Then we can employ the compatibility condition Eq. (2.22) or Eq. (2.23) to get the term $\overline{A}$ in Eq. (2.18). Finally, the numerical flux $\widehat{\mathbf{G}}(x_{i+\frac{1}{2}},y_*,t)$ can be obtained by taking the moments of $u\psi$ to the distribution function f given by Eq. (2.12).

2.4. Limiting procedure and boundary conditions

For the compressible flow simulations by the RKDG method, the direct update of the numerical solution will generate numerical oscillations across strong shock waves. In order to eliminate these oscillations, the non-linear limiter, usually used in the FV method, has to be used in the RKDG method as well. In this paper, in 1D case, we use the Hermite WENO limiter [18] proposed by Qiu and Shu recently. In 2D case, for the rectangular elements a similar limiting procedure to that in [10] is employed. Consider a scalar equation $w_t + G_x + H_y = 0$ in 2D space, for P^1 scheme the approximate solution w^h inside the element $I_{i,j}$ is known as

$$w^h(\mathbf{x}, t) = \sum_{l=0}^{2} w_{i,j}^l(t)\phi_{i,j}^l(\mathbf{x}) \quad \text{for } \mathbf{x} \in I_{i,j}. \tag{2.34}$$

For $w_{i,j}^1$, the slope limiter used is

$$\tilde{w}_{i,j}^1 = \bar{m}\left(w_{i,j}^1, w_{i+1,j}^0 - w_{i,j}^0, w_{i,j}^0 - w_{i-1,j}^0\right), \tag{2.35}$$

where the function $\bar{m}$ is the TVB corrected *minmod* function [20] defined by

$$\bar{m}(a_1, a_2, a_3) = \begin{cases} a_1 & \text{if } |a_1| \leqslant M\Delta x_i^2, \\ m(a_1, a_2, a_3) & \text{otherwise.} \end{cases} \tag{2.36}$$

Here the *minmod* function m is given by

$$m(a_1, a_2, a_3) = \begin{cases} s\min(|a_1|, |a_2|, |a_3|) & \text{if } s = \text{sign}(a_1) = \text{sign}(a_2) = \text{sign}(a_3), \\ 0 & \text{otherwise.} \end{cases} \tag{2.37}$$

Similarly, $w_{i,j}^2$ is limited by

$$\tilde{w}_{i,j}^2 = \bar{m}(w_{i,j}^2, w_{i,j+1}^0 - w_{i,j}^0, w_{i,j}^0 - w_{i,j-1}^0), \tag{2.38}$$

where Δx_i in Eq. (2.36) is changed to Δy_j. For P^2 parts, no limiting is imposed *if* $\tilde{w}_{i,j}^1 = w_{i,j}^1$ and $\tilde{w}_{i,j}^2 = w_{i,j}^2$; otherwise we remove all higher-order parts, i.e., $w_{i,j}^3$, $w_{i,j}^4$, and $w_{i,j}^5$, in the approximate solution. For both 1D and 2D cases, the componentwise limiting operator is used after each Runge–Kutta or TVD-RK [19] inner stage.

Now we describe the treatment of boundary conditions. For the adiabatic wall, the no-slip boundary condition for the velocity field is imposed by reversing the velocities in the ghost cell from the sate in the interior region, and the mass and energy densities are put to be symmetric around the wall. For the isothermal wall, where the boundary temperature is fixed, we use the condition of no net mass flux transport across the boundary [24] to construct the flow states in the ghost cell, where the spacial derivatives are calculated from the data around the wall by approximation consistent with the accuracy requirement. For example, a parabolic reconstruction for the flow variables around the wall has to be used for the P^2 scheme, whereas the linear approximation is implemented in the P^1 case. At the inflow/outflow boundaries, the flow states at the external boundary are computed from the available data and Riemann invariants, and the spacial derivatives there are also obtained by appropriate approximation with the given boundary condition.

3. Numerical experiments

The present RKDG method will be tested in both 1D and 2D problems. We use the two-stage TVD-RK time stepping method [19] for P^1 case and the three-stage one for both P^2 and P^3 cases, the CFL number is 0.2 for P^1 case and 0.15 for P^2 case.

3.1. Accuracy test

The first test is to solve the Navier–Stokes equations with the following initial data:

$$\rho(x,0) = 1 + 0.2\sin(\pi x), \quad U(x,0) = 1, \quad p(x,0) = 1. \tag{3.1}$$

The dynamical viscosity coefficient is taken by a value $\mu = 0.0005$. The Prandtl number is $Pr = 2/3$ and the specific heat ratio is $\gamma = 5/3$. The computational domain is $x \in [0,2]$ and the periodic boundary condition is used. We compute the viscous solution up to time $t = 2$ with a small time step to guarantee that the spatial discretization error dominates. No limiter is used in this case. Since there is no exact solution for this problem, we evaluate the numerical error between the solutions by two successively refined meshes and use the error to estimate the numerical convergence rates. The results are shown in Tables 1–3. From these results we can clearly notice that a $(k+1)$th-order convergence rate can be obtained for P^k $(k = 1,2,3)$ schemes for smooth solutions.

3.2. Couette flow

The Couette flow with a temperature gradient provides a good test for the RKDG method to describe the viscous heat-conducting flow. With the bottom wall fixed, the top boundary is moving at a speed U in the horizontal direction. The temperatures at the bottom and top are fixed with values T_0 and T_1. Under the assumption of constant viscosity and heat conduction coefficients and in the incompressible limit, a steady state analytical temperature distribution can be obtained,

$$\frac{T - T_0}{T_1 - T_0} = \frac{y}{H} + \frac{PrEc}{2}\frac{y}{H}\left(1 - \frac{y}{H}\right), \tag{3.2}$$

where H is the height of the channel, Pr is the Prandtl number, Ec is the Eckert number $Ec = U^2/C_p(T_1 - T_0)$, and C_p is the specific heat at constant pressure.

We set up the simulation as a 1D problem in the y-direction. There are five cells used in this direction from 0 to 5 with $H = 5$ and $\Delta y = 1$. The moving velocity at the top boundary in the x-direction is $U = 0.1$. The dynamical viscosity coefficient is taken as $\mu = 0.1$. The initial density and Mach number of the gas inside

Table 1
The error and convergence order for P^1 case

N	L^∞-error	Order	L^1-error	Order	L^2-error	Order
10	3.05E−2	–	1.76E−2	–	1.99E−2	–
20	5.68E−3	2.42	3.36E−3	2.39	3.79E−3	2.39
40	1.03E−3	2.46	6.31E−4	2.41	7.07E−4	2.42
80	2.08E−4	2.31	1.28E−4	2.30	1.44E−4	2.30

Table 2
The error and convergence order for P^2 case

N	L^∞-error	Order	L^1-error	Order	L^2-error	Order
10	2.48E−3	–	1.51E−3	–	1.62E−3	–
20	2.76E−4	3.16	1.66E−4	3.18	1.86E−4	3.12
40	2.50E−5	3.47	1.54E−5	3.43	1.73E−5	3.42
80	2.54E−6	3.30	1.47E−6	3.39	1.64E−6	3.40

Table 3
The error and convergence order for P^3 case

N	L^∞-error	Order	L^1-error	Order	L^2-error	Order
10	9.05E−5	–	5.37E−5	–	5.67E−5	–
20	8.89E−6	3.35	4.23E−6	3.67	4.90E−6	3.53
40	4.90E−7	4.18	2.81E−7	3.91	3.17E−7	3.95
80	3.26E−8	3.91	1.42E−8	4.30	1.70E−8	4.22

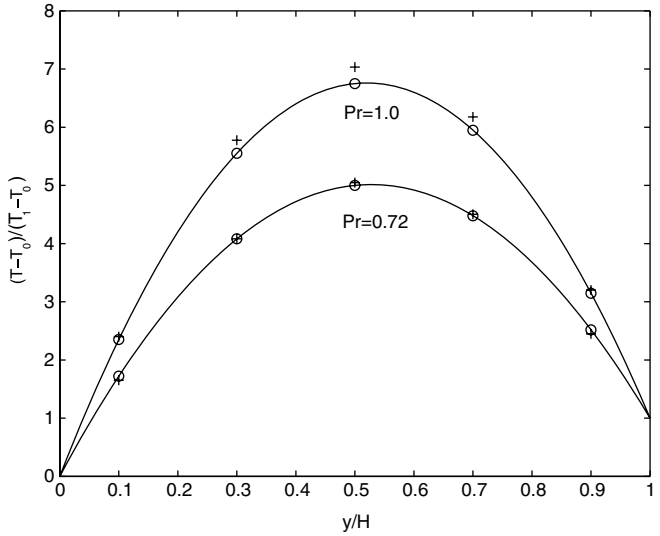

Fig. 1. Temperature ratio $(T - T_0)/(T_1 - T_0)$ in the Couette flow with $\gamma = 5/3$, $Ec = 50$. The solid line is the analytical solution given by Eq. (3.2), the plus symbol is the numerical solution by P^1 method and the circle symbol is by P^2 one.

the channel are 1.0 and 0.1, respectively. In this case the fluid in the channel is almost incompressible. The isothermal no-slip boundary conditions are implemented at both ends. We have tested the RKDG method with a wide range of parameters. Here some of them are presented: (i) specific heat ratio $\gamma = 5/3$, 7/5, (ii) different Prandtl number $Pr = 0.72$, 1.0, (iii) different Eckert number $Ec = 10$, 50. The results without limiter are shown in Figs. 1 and 2. From these figures, we see that the numerical results recover the analytical solutions very well with the variations of all these parameters, and the Prandtl number fix does modify the heat conduction term correctly. It is also clearly shown that the higher-order P^2 scheme gives more accurate solutions than the lower-order P^1 scheme with the same mesh size. If we further refine the mesh, the difference between the numerical solution from P^1 and P^2 cases is indistinguishable and both accurately recover the analytical solution.

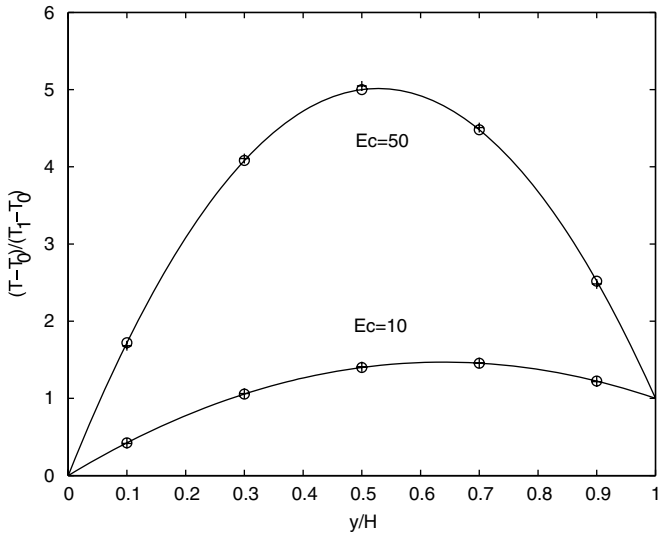

Fig. 2. Temperature ratio $(T - T_0)/(T_1 - T_0)$ in the Couette flow with $\gamma = 7/5$, $Pr = 0.72$. The solid line is the analytical solution given by Eq. (3.2), the plus symbol is the numerical solution by P^1 method and the circle symbol is by P^2 one.

3.3. Navier–Stokes shock structure

The third test is the Navier–Stokes shock structure calculation. Although it is well known that in the high Mach number case the Navier–Stokes solutions do not give the physically realistic shock wave profile, it is still a useful case in establishing and testing a valid solver for the Navier–Stokes equations. Even though the shock structure is well-resolved in this case, due to the highly non-equilibrium state inside the shock layer, its accurate calculation bears large requirement on the accuracy and robustness of the numerical method. The profile of a normal shock structure, and the correct capturing of the viscous stress and heat conduction inside the shock layer represent a good test for the viscous flow solver.

The shock structure calculated is for a monotonic gas with $\gamma = 5/3$ and a dynamical viscosity coefficient $\mu \sim T^{0.8}$, where T is the temperature. The upstream Mach number $M = 1.5$ and the Prandtl number $Pr = 2/3$ are used in this test. The dynamical viscosity coefficient at the upstream keeps a constant value $\mu_{-\infty} = 0.0005$. The reference solution is obtained by directly integrating the steady state Navier–Stokes equations, and the Matlab programs are provided in Appendix C of [24]. Because the normal stress and the heat

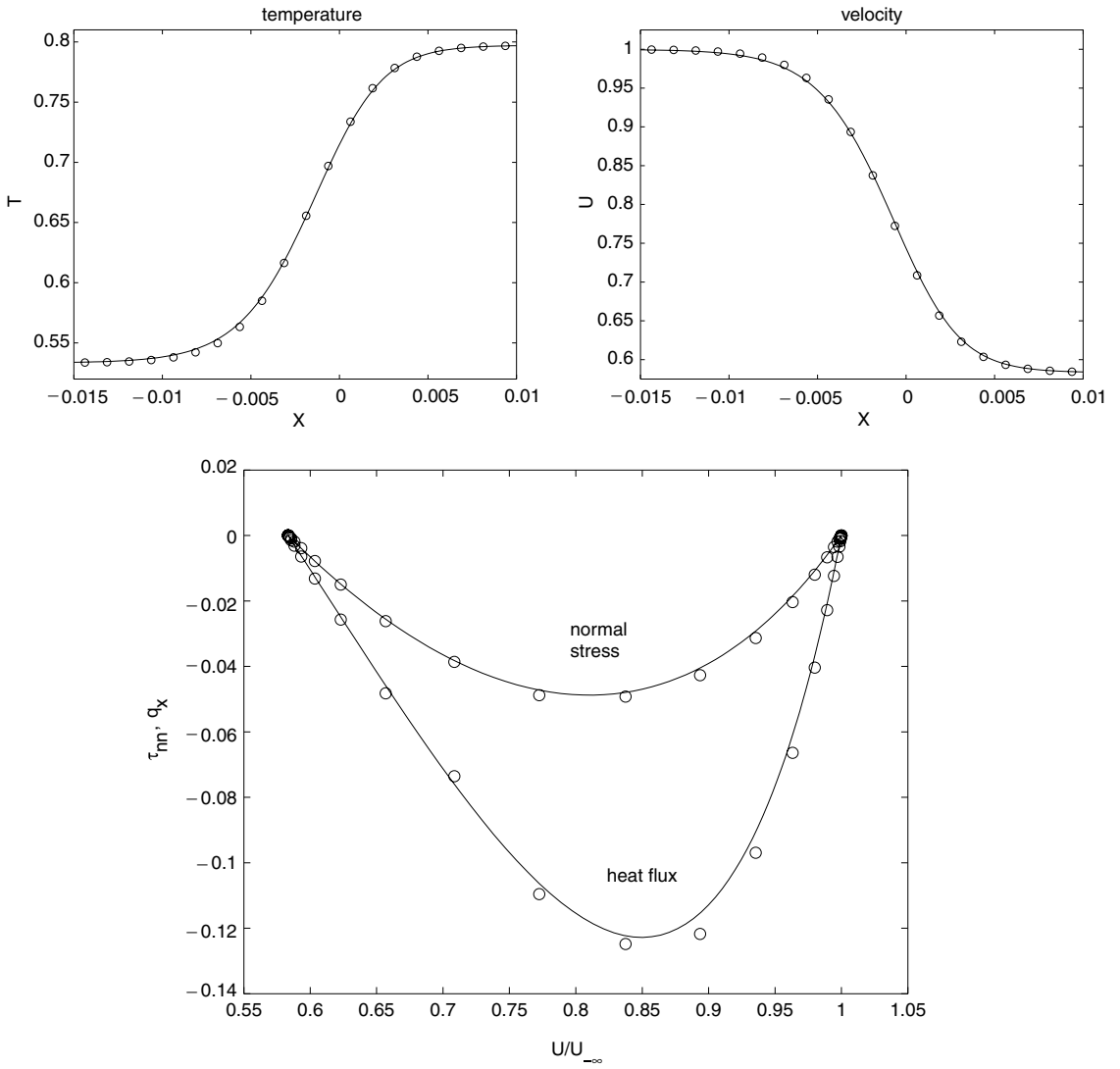

Fig. 3. Navier–Stokes shock structure calculation, P^1 case.

flux seem to show the greatest numerical sensitivity, these are selected to display. Therefore, the profiles of the temperature T and the fluid velocity U across the shock layer, as well as the normal stress and the heat flux defined by

$$\tau_{nn} = \frac{4}{3}\mu\frac{U_x}{2p}, \quad q_x = -\frac{5}{4}\frac{\mu}{Pr}\frac{T_x}{pc}, \tag{3.3}$$

versus fluid velocity $U/U_{-\infty}$, are calculated. In the above equation p is the pressure and c is the speed of sound.

The mesh size used is $\Delta x = 1/800$ for both P^1 and P^2 cases. The results calculated by the second-order P^1 case are presented in Fig. 3 and those by the third-order P^2 case are shown in Fig. 4. From these results, we can see that the shock structure is calculated accurately with a reasonable number of grid points inside the shock layer. Moreover, the third-order scheme gives more accurate results than the second-order scheme, especially in the normal stress and heat flux solutions.

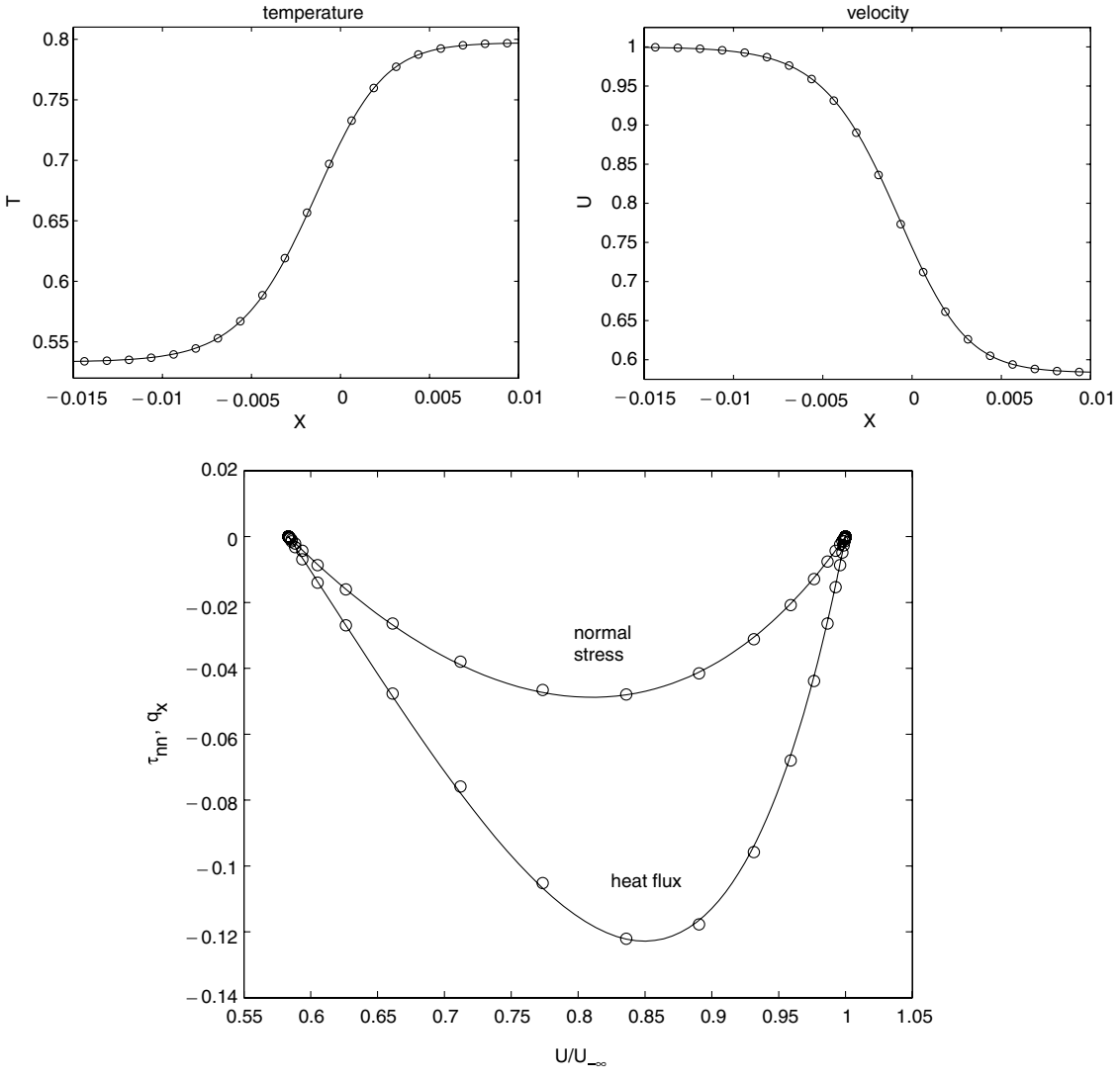

Fig. 4. Navier–Stokes shock structure calculation, P^2 case.

3.4. Shock tube problem

In the fourth example, in order to further test the RKDG method in capturing the Navier–Stokes solutions in the unsteady case, we calculate the well-known Sod's test directly by solving the Navier–Stokes equations with $\gamma = 1.4$ and $Pr = 2/3$. The cell size used here is $\Delta x = 1/200$. Fig. 5 gives the results with a kinematic viscosity coefficient $v = 0.0005/\rho\sqrt{\lambda}$, where λ is related to the temperature in the local equilibrium distribution function g_0. The solid lines there are the reference solutions calculated by the FV BGK scheme [24] with a much refined mesh size $\Delta x = 1/1200$. In this case, due to the large viscosity coefficient both the shock structure and the contact wave are well-resolved by the cell size used and both of them are captured accurately. Again the higher-order scheme gives more accurate results than the lower-order scheme, which can be clearly seen in both the velocity distributions in Fig. 5 and the zoom-in views of the density distributions around the shock wave in Fig. 6. The subcell solution presented in Fig. 6 also demonstrates this fact clearly. The results with a much smaller viscosity coefficient $v = 0.00005/\rho\sqrt{\lambda}$ are also presented in Fig. 7. Here the shock structure cannot be resolved by the large cell size used, and the RKDG method becomes a shock capturing scheme. The shock transition is purely constructed from the numerical dissipation, which is much wider than the physical one determined from the above physical viscosity.

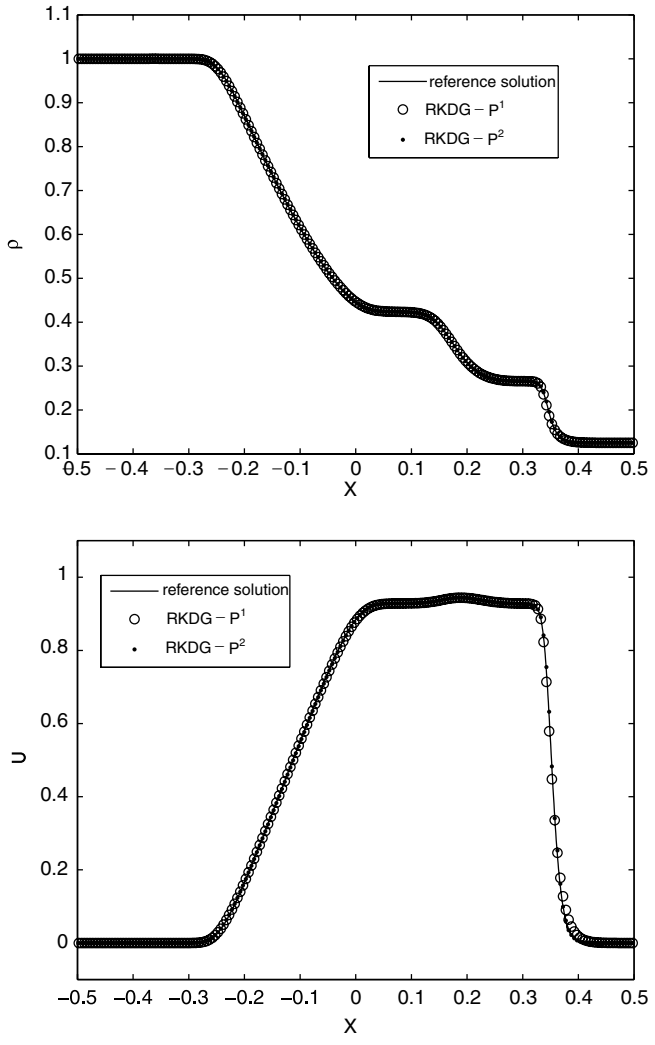

Fig. 5. Shock tube test for the Navier–Stokes equations with kinematic viscosity coefficient $v = 0.0005/\rho\sqrt{\lambda}$.

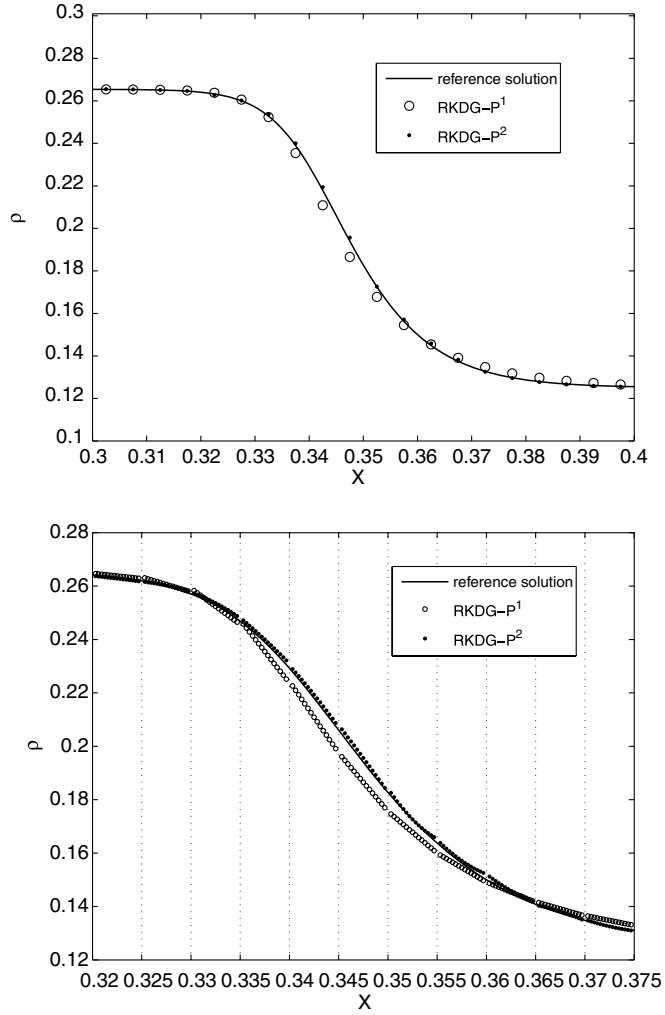

Fig. 6. The zoom-in views of the density distributions around the shock wave in shock tube test with $v = 0.0005/\rho\sqrt{\lambda}$. The upper one is the same as that in Fig. 5, where only the values at cell centers are displayed. The lower one presents the values at 15 equally spaced positions inside each cell, the so-called subcell solution.

3.5. Laminar boundary layer

The next numerical example is the laminar boundary layer over a flat plate with the length L. The Mach number is $M = 0.2$ and the Reynolds number based on the upstream flow states and the length L is $Re = 10^5$. A rectangular mesh with 120×30 cells is used and the mesh distribution is shown in Fig. 8. The mesh size ranges from $\Delta x/L = 1.0 \times 10^{-3}$ at the leading edge to $\Delta x/L = 4.9 \times 10^{-2}$ at the end of the plate in the x-direction, and from $\Delta y/L = 6.6 \times 10^{-4}$ near the wall to $\Delta y/L = 0.11$ at the upper boundary in the y-direction. The U velocity contours at the steady state computed by the P^2 scheme are shown in Fig. 9. We have also compared the numerical results with the theoretical ones given by the well-known Blasius solution in case of incompressible flow. The U velocity distributions along three different vertical lines are shown in Figs. 10 and 11. From these figures, we can see that the numerical solutions by both P^1 and P^2 schemes recover the theoretical solution accurately, even with as few as four grid points in the boundary layer. The computed skin friction coefficient along the flat plate is shown in Fig. 12, where a very good agreement with the Blasius solution is obtained. The logarithmic plot of the skin friction coefficient in Fig. 13 shows that the higher-order P^2 scheme performs better than the lower-order P^1 scheme in both the leading edge and the outflow region. Similar observation is obtained in [1].

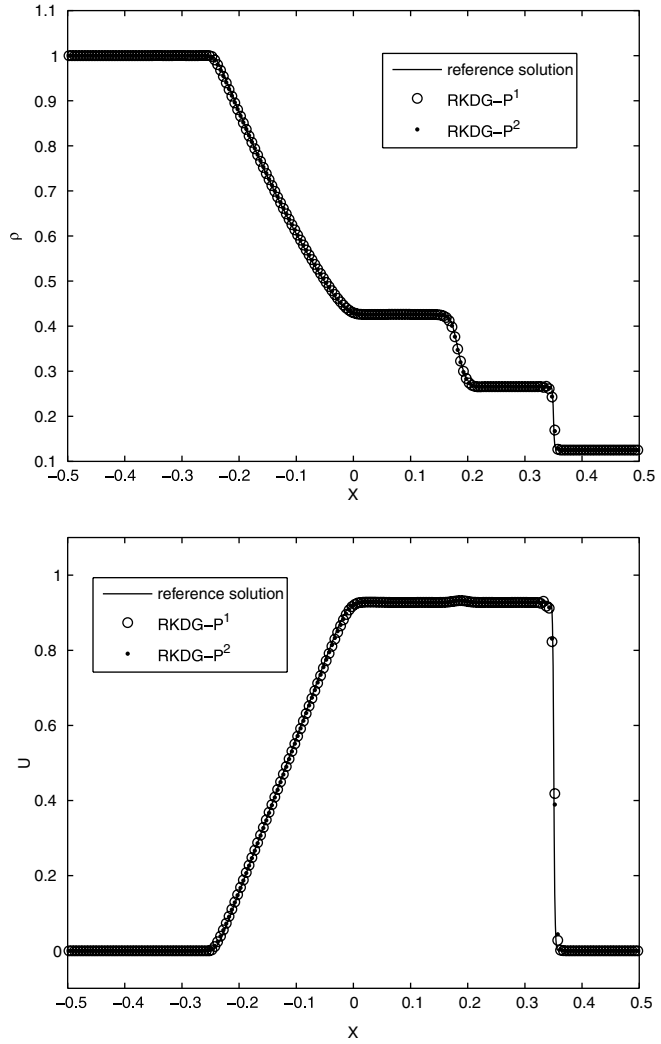

Fig. 7. Shock tube test for the Navier–Stokes equations with kinematic viscosity coefficient $v = 0.00005/\rho\sqrt{\lambda}$.

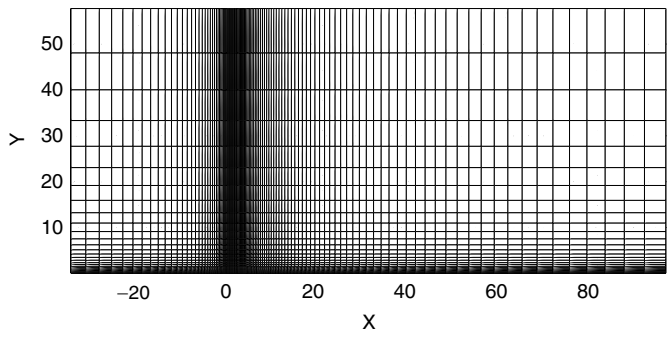

Fig. 8. Mesh distribution for laminar boundary layer problem.

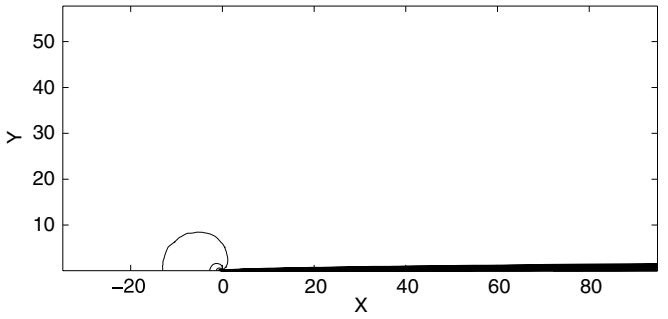

Fig. 9. Laminar boundary layer problem. One hundred equally spaced contours of the fluid velocity $U/U_{-\infty}$ from 0 to 1.0061 from P^2 calculation.

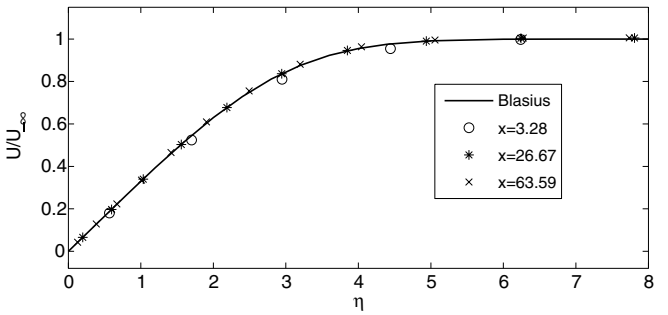

Fig. 10. Laminar boundary layer problem. U velocity distributions along three vertical lines by P^1 case.

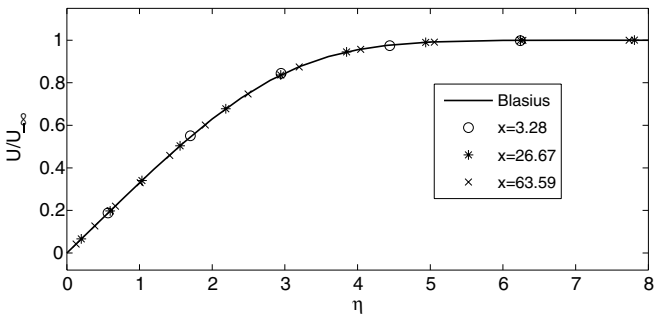

Fig. 11. Laminar boundary layer problem. U velocity distributions along three vertical lines by P^2 case.

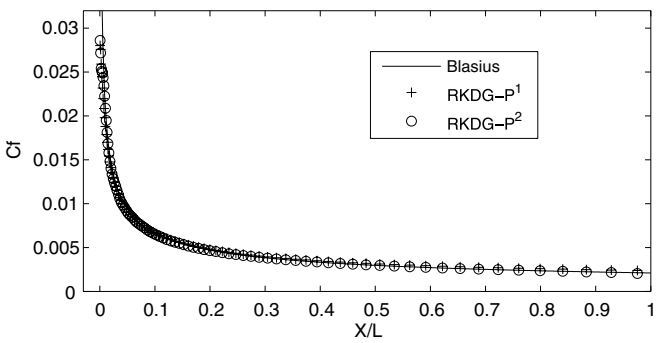

Fig. 12. Laminar boundary layer problem. Skin friction coefficient distribution along the flat plate.

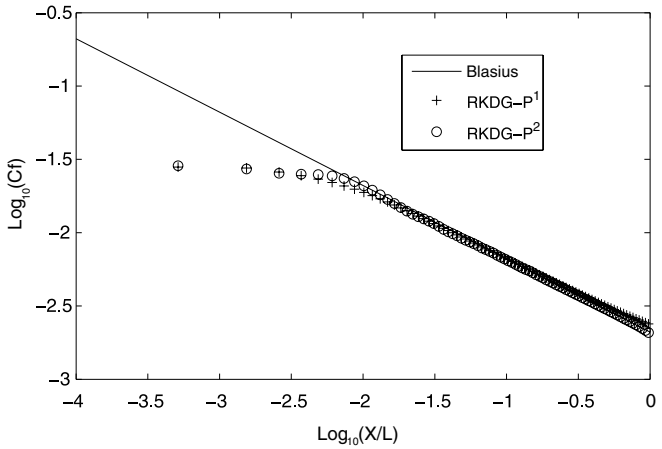

Fig. 13. Laminar boundary layer problem. Logarithmic plot of the skin friction coefficient distribution along the flat plate.

3.6. Shock boundary layer interaction

The final test deals with the interaction of an oblique shock with a laminar boundary layer, which has been computed by Bassi and Rebay with an implicit high-order discontinuous Galerkin method [2]. The shock makes a 32.6° angle with the wall, which is located at $y = 0$ and $x \geqslant 0$, and hits the boundary layer on the

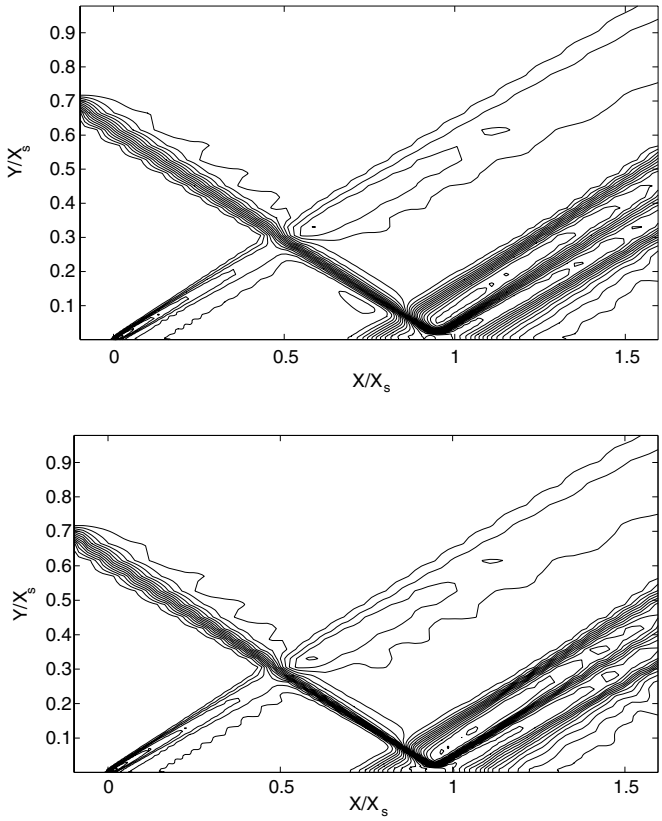

Fig. 14. Shock boundary layer interaction. Thirty equally spaced contours of pressure $p/p_{-\infty}$ from 0.997 to 1.411 by P^1 (upper) and P^2 (lower) cases.

wall at $X_s = 10$. The Mach number of the shock wave is equal to 2 and the Reynolds number based on the upstream flow condition and the characteristic length X_s is equal to 2.96×10^5. The dynamical viscosity μ is computed according to the Sutherland's law for the gas with $\gamma = 1.4$ and $Pr = 0.72$. The computation was carried out on a rectangular domain $[-1.05 \leqslant x \leqslant 16.09] \times [0 \leqslant y \leqslant 10.16]$. A nonuniform mesh with 106×73 cells, similar to the laminar boundary layer problem, is constructed. The mesh size varies from $\Delta x/X_s = 1.0 \times 10^{-2}$ around $x = 0$ to $\Delta x/X_s = 2.6 \times 10^{-2}$ at the end of the plate in the x-direction, and from $\Delta y/X_s = 3.2 \times 10^{-4}$ around $y = 0$ to $\Delta y/X_s = 7.6 \times 10^{-2}$ at the upper boundary in the y-direction. The pressure contours computed by the P^1 and P^2 schemes are presented in Fig. 14. In this case the shock structure cannot be well-resolved by the current mesh size and the RKDG method turns out to be a shock capturing one in terms of the shock. As expected, the P^2 scheme gives a shaper numerical shock transition than that from P^1 scheme due to the less numerical dissipation introduced by weaker discontinuities at the cell interfaces. On the other hand, the boundary layer can be resolved under the present mesh. The skin friction and pressure distributions at the plate surface are shown in Fig. 15, where a fair agreement with the experimental data [13] is obtained for both P^1 and P^2 schemes, and the P^2 scheme performs slightly better than the P^1 scheme. Our numerical results are comparable with those in [17]. The main discrepancy between the experimental and numerical results is probably due to the assumption that the flow is laminar whereas the real physical one could be turbulent.

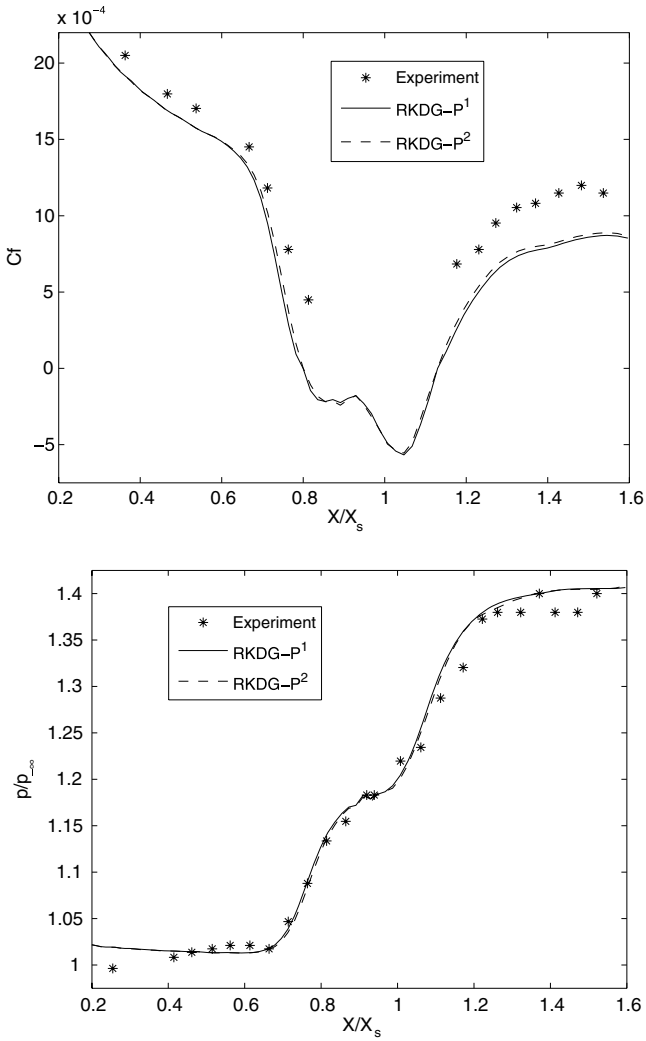

Fig. 15. Shock boundary layer interaction. Skin friction (upper) and pressure (lower) distributions at the plate surface.

4. Conclusions

In this paper, a RKDG method for the viscous flow computation has been presented. The construction of the RKDG method is based on a gas-kinetic formulation, which combines the convective and dissipative terms together in a single gas distribution function. Due to the intrinsic connection between the gas-kinetic BGK model and the Navier–Stokes equations, the Navier–Stokes flux is automatically obtained by the method. The current RKDG method has good shock capturing capacity, where the numerical dissipation introduced from the numerical flux at the cell interface is controlled adaptively by a hybrid parameter in the current approach. The RKDG method works very well for all test cases presented. The higher-order P^2 scheme does give a more accurate solution than that from the lower-order P^1 scheme, especially in the well-resolved cases. In terms of the computational cost, the present RKDG method is more expensive, especially in the multidimensional cases, than the finite volume gas-kinetic BGK method for the Navier–Stokes equations. For the RKDG methods, the limiting procedure plays an important role for the quality of numerical solutions and its formulation is sophisticated in the cases with strong discontinuities. Generally speaking, both the numerical flux and the limiting procedure are needed to bring numerical dissipation into the viscous solutions. This kind of dissipation is unavoidable because with limited cell size we cannot fully resolve the physical solutions, such as the shock structure, the leading edge of the boundary layer, or the small scale turbulent flow, even though we are claiming to solve the viscous governing equations.

Acknowledgments

The authors would like to thank the reviewers for their constructive comments, which improve the manuscript greatly. Thanks also go to Prof. C.W. Shu, Prof. H.Z. Tang and Dr. T. Zhou for their helpful discussions about RKDG methods. The work described in this paper was substantially supported by grants from the Research Grants Council of the Hong Kong Special Administrative region, China (Project No. HKUST6210/05E and 6214/06E).

References

[1] F. Bassi, S. Rebay, A high-order accurate discontinuous finite element method for the numerical solution of the compressible Navier–Stokes equations, J. Comput. Phys. 131 (1997) 267.
[2] F. Bassi, S. Rebay, An implicit high-order discontinuous Galerkin method for the steady state compressible Navier–Stokes equations, Computational Fluid Dynamics '98, Proceedings of the Fourth European Computational Fluid Dynamics Conference, vol. 2, 1998, p. 1226.
[3] P.L. Bhatnagar, E.P. Gross, M. Krook, A model for collision processes in gases I: Small amplitude processes in charged and neutral one-component systems, Phys. Rev. 94 (1954) 511.
[4] S.Y. Chou, D. Baganoff, Kinetic flux-vector splitting for the Navier–Stokes equations, J. Comput. Phys. 130 (1997) 217.
[5] D.N. Arnold, F. Brezzi, B. Cockburn, L.D. Marini, Unified analysis of discontinuous Galerkin methods for elliptic problems, SIAM J. Numer. Anal. 39 (2002) 1749.
[6] B. Cockburn, G.E. Karniadakis, C.W. Shu, The development of discontinuous Galerkin methods, in: B. Cockburn, G.E. Karniadakis, C.W. Shu (Eds.), Discontinuous Galerkin Methods: Theory, Computation and Applications, Springer, Berlin, 2000.
[7] B. Cockburn, C.W. Shu, TVB Runge–Kutta local projection discontinuous Galerkin finite element method for scalar conservation laws II: General framework, Math. Comput. 52 (1989) 411.
[8] B. Cockburn, S.Y. Lin, C.W. Shu, TVB Runge–Kutta local projection discontinuous Galerkin finite element method for conservation laws III: One dimensional systems, J. Comput. Phys. 84 (1989) 90.
[9] B. Cockburn, S. Hou, C.W. Shu, TVB Runge–Kutta local projection discontinuous Galerkin finite element method for conservation laws IV: The multidimensional case, Math. Comput. 54 (1990) 545.
[10] B. Cockburn, C.W. Shu, The Runge–Kutta discontinuous Galerkin method for conservation laws V: Multidimensional systems, J. Comput. Phys. 141 (1998) 199.
[11] B. Cockburn, C.W. Shu, The local discontinuous Galerkin method for time-dependent convection–diffusion systems, SIAM J. Numer. Anal. 35 (1998) 2440.
[12] B. Cockburn, C.W. Shu, Runge–Kutta discontinuous Galerkin method for convection-dominated problems, J. Sci. Comput. 16 (2001) 173.
[13] R.J. Hakkinen, L. Greber, L. Trilling, S.S. Abarbanel, The interaction of an oblique shock wave with a laminar boundary layer, NASA Memo. 2-18-59W, NASA, 1959.
[14] C.E. Baumann, J.T. Oden, A discontinuous hp finite element method for the Euler and Navier–Stokes equations, Int. J. Numer. Methods Fluids 31 (1999) 79.

[15] H.Z. Tang, G. Warnecke, A Runge–Kutta discontinuous Galerkin method for the Euler equations, Comput. Fluids 34 (2005) 375.
[16] T. Ohwada, On the construction of kinetic schemes, J. Comput. Phys. 177 (2002) 156.
[17] T. Ohwada, S. Fukata, Simple derivation of high-resolution schemes for compressible flows by kinetic approach, J. Comput. Phys. 211 (2006) 424.
[18] J. Qiu, C.W. Shu, Hermite WENO schemes and their application as limiters for Runge–Kutta discontinuous Galerkin method: one dimensional case, J. Comput. Phys. 193 (2004) 115.
[19] C.W. Shu, S. Osher, Efficient implementation of essential non-oscillatory shock capturing schemes, II, J. Comput. Phys. 83 (1989) 32.
[20] C.W. Shu, TVB uniformly high-order schemes for conservation laws, Math. Comput. 49 (1987) 105.
[21] B. van Leer, Towards the ultimate conservative difference scheme IV. A new approach to numerical convection, J. Comput. Phys. 23 (1977) 276.
[22] B. van Leer, S. Nomura, Discontinuous Galerkin for diffusion, AIAA-2005-5108, 17th AIAA Computational Fluid Dynamics Conference, 2005.
[23] K. Xu, Gas-kinetic schemes for unsteady compressible flow simulations, VKI for Fluid Dynamics Lecture Series 1998-03, 1998.
[24] K. Xu, A gas-kinetic BGK scheme for the Navier–Stokes equations and its connection with artificial dissipation and Godunov method, J. Comput. Phys. 171 (2001) 289.
[25] K. Xu and A. Jameson, Gas-kinetic relaxation (BGK-type) schemes for the compressible Euler equations, AIAA-95-1736, 12th AIAA Computational Fluid Dynamics Conference, 1995.
[26] K. Xu, Z.W. Li, Dissipative mechanism in Godunov-type schemes, Int. J. Numer. Methods Fluids 37 (2001) 1.
[27] K. Xu, M.L. Mao, L. Tang, A multidimensional gas-kinetic BGK scheme for hypersonic viscous flow, J. Comput. Phys. 203 (2005) 405.
[28] K. Xu, Discontinuous Galerkin BGK method for viscous flow equations: one-dimensional systems, SIAM J. Sci. Comput. 23 (2004) 1941.